

## Numerical modeling analysis of short-offset electric-field measurements with a vertical electric dipole source in complex offshore environments

Evan Schankee Um<sup>1</sup>, David L. Alumbaugh<sup>2</sup>, Jerry M. Harris<sup>3</sup>, and Jiuping Chen<sup>4</sup>

### ABSTRACT

We simulated and analyzed short-offset transient electric-field measurements excited by a vertical electric dipole (VED) source over complex 3D offshore models. A finite-element time-domain modeling algorithm was used to efficiently model complex offshore structures. Using a series of cross-sectional snapshots of transient electric fields in the complex offshore models, we examined the characteristics of the short-offset seafloor electric-field measurements. The numerical modeling analysis indicated that the short-offset horizontal electric-field ( $E_x$ ) measurements are very sensitive to subtle multidimensional seafloor

topography near a VED source and can show a sign reversal at late times. The sign reversal occurs because the VED source is no longer normal to the seafloor. The occurrence of the sign reversal limits the application of the 1D inversion to the  $E_x$  measurements, even at a short source-receiver offset. In contrast, the short-offset vertical electric-field ( $E_z$ ) measurements are robust to subtle seafloor topography around the source, and can be interpreted using the 1D inversion. The 1D inversion of the short-offset  $E_z$  measurements over the complex 3D offshore models shows that the measurements lack the resolution of the thickness and the resistivity of a hydrocarbon reservoir and a salt dome, but can provide useful insights into their lateral extent.

### INTRODUCTION

The marine controlled-source electromagnetic (CSEM) method first succeeded in identifying hydrocarbon reservoirs in offshore Angola (Eidesmo et al., 2002; Ellingsrud et al., 2002). Since then, the CSEM method has rapidly evolved from an anomaly detection tool to a sophisticated multidimensional imaging-based tool (Gribenko and Zhdanov, 2007; Abubakar et al., 2008; Commer and Newman, 2008). The CSEM method consists of an electric dipole source and an array of seafloor receivers. The source is typically towed just a few tens of meters above the seafloor to ensure maximum coupling between the generated electromagnetic (EM) fields and the seabed.

For typical exploration purposes, the CSEM method employs a horizontal electric dipole (HED) source and is operated in the frequency domain. The sensitivity of the frequency-domain CSEM (FDCSEM) method to a reservoir is controlled not only by its acquisition layouts but also by the seawater depth (Um and

Alumbaugh, 2007; Chave, 2009). As the seawater depth gradually decreases, the airwave is increasingly less attenuated through the seawater column. When the airwave is strong enough to mask a reservoir response at seafloor receivers, the FDCSEM method loses its sensitivity to the reservoir. Several approaches have been proposed to overcome the airwave effect in a shallow offshore environment, but the effectiveness of these approaches depends on characteristics of the noise and reservoir signal levels relative to the airwave (Weidelt, 2007; Chen and Alumbaugh, 2011).

An alternative to the FDCSEM method in shallow water is the time-domain CSEM (TDCSEM) method. The TDCSEM method was originally used for crustal research and methane hydrates mapping (Cheesman et al., 1987; Everett and Edwards, 1992; Edwards, 1997) but has recently been recognized as an alternative to the FDCSEM method in shallow water (Weiss, 2007). When a transient HED source is excited, some EM fields diffuse upward through a shallow water column, propagate through the atmosphere, and diffuse back through the water column. The shallower the water

Manuscript received by the Editor 1 November 2011; revised manuscript received 9 March 2012; published online 8 August 2012.

<sup>1</sup>Lawrence Berkeley National Laboratory, Earth Sciences Division, Geophysics Department, Berkeley, California, USA. E-mail: evanum@gmail.com.

<sup>2</sup>Chevron Energy Technology, San Ramon, California, USA. E-mail: DAlumbaugh@chevron.com.

<sup>3</sup>Stanford University, Geophysics Department, Stanford, California, USA. E-mail: jerry.harris@stanford.edu.

<sup>4</sup>Schlumberger-EMI, Berkeley, California, USA. E-mail: jchen16@slb.com.

© 2012 Society of Exploration Geophysicists. All rights reserved.

column is, the earlier the airwave arrives at receiver locations. In contrast, a deep reservoir response arrives slowly through the conductive seabed. Therefore, in shallow water, the airwave response can be separated from the reservoir response due to different arrival times of the two responses.

Recently, a new TCSEM method using a vertical electric dipole (VED) source has been developed (Holten et al., 2009; Flekkoy et al., 2010). Unlike the conventional TDCSEM method described above, the new TDCSEM method with the VED source utilizes relatively short source-receiver offsets (e.g., 500 to 1500 m). The transient currents originating from the lower tip of the VED source diffuse directly downward to the seabed. The currents interact with a resistive structure (e.g., hydrocarbon reservoirs) below the source. The resulting anomalous EM fields are measured at short offsets and are utilized to interpret deep seabed structures.

Modeling studies of the TDCSEM method with the VED source have been recently presented (Scholl and Edwards, 2007; Alumbaugh et al., 2010; Cuevas and Alumbaugh, 2011). However, the studies have been carried out with seabed models of limited geometric complexity. Although the simplified seabed models can be useful under some circumstances (e.g., to investigate the basic physics of the TDCSEM method), they may not fully explain representative TDCSEM exploration scenarios associated with highly complex and subtle offshore geology. The existing TDCSEM modeling studies also focus mainly on deepwater applications to hydrocarbon explorations.

In this paper, we present a 3D numerical modeling analysis of the short-offset TDCSEM method with the VED source in relatively shallow (less than about 400 m) offshore models that include complex 3D bathymetry, a reservoir, and a salt dome. To simulate TDCSEM method over such complex geological structures, we utilize 3D finite-element time-domain (FETD) algorithms (Um et al., 2010). By utilizing unstructured tetrahedral meshes, the FETD algorithm accurately and efficiently discretizes the complex geological structures. The primary goals of this FETD modeling study are to analyze characteristics of short-offset electric-field measurements with a VED source in complex and subtle multidimensional offshore environments; to examine the sensitivity and the resolution of the short-offset measurements to a localized hydrocarbon reservoir close to a large-scale salt dome; and to demonstrate the usefulness and the limitation of 1D inversion over complex 3D seabed structures when the short-offset TDCSEM configurations are employed. At least as far as we know, such complex and realistic 3D time-domain CSEM modeling studies with short-offset configurations have never appeared in the literature.

The remainder of this paper is organized as follows. To begin, we briefly describe the construction of finite-element-based electrical-conductivity models from a seismic offshore model that consists of complex seabed structures. Using these offshore models, we carry out the following numerical experiments. Initially, we visualize the diffusion of transient electric fields on the cross section of the offshore models and analyze the interaction of the electric fields with the irregular seafloor, a reservoir, and a salt dome. Then, we investigate the sensitivity of the short-offset electric-field measurements to the reservoir and the salt dome. The influence of subtle seafloor topography on the short-offset measurements is examined. Finally, we attempt to invert short-offset 3D modeling data using a 1D inversion and discuss the results.

## CONSTRUCTION OF FINITE-ELEMENT OFFSHORE MODELS

To construct realistic finite-element (FE) offshore models, we utilize the SEG salt model (Aminzadeh et al., 1997). The SEG model is  $13.5 \times 13.5 \times 4.2$  km in the  $x$ -,  $y$ - and  $z$ -directions, respectively, and its grid size is 20 m in all three directions. The SEG model primarily consists of three structures: the complex seabed, the irregular seafloor topography, and the salt dome. Among the three structures, the irregular seafloor and the salt dome are imported to the FE modeling space. The complex seabed stratigraphy is not inserted into the FE modeling space due to computation costs. The seabed is assumed homogeneous unless the salt dome and/or the reservoir are inserted.

To convert the gridded salt dome and seafloor topography structures into corresponding FE structures, the surface coordinates of the structures are sampled at 300-m intervals. Then, the 3D surfaces of each structure are reconstructed in the 3D FE modeling space using a Delaunay algorithm (Barber et al., 1996). During the reconstruction processes, if the sampling interval is too large (e.g., 1 km), we observe that the reconstructed structure is distorted from the original structures. However, when the sampling interval is too small (e.g., 40 m), the reconstruction processes are computationally intensive and become intractable on a modern personal computer (e.g., 2.8 GHz Intel Duo processor with 8-GB memory). As a compromise, we sample the structures every 300 m in the  $x$ - and  $y$ -directions. The resulting reconstructed 3D surfaces of the seafloor and the salt dome are shown in Figure 1a and 1b.

Starting with this reconstructed model, we introduce two changes that allow the model to accommodate more realistic TDCSEM survey environments. First, we increase the seawater depth by 200 m. Note that the seawater depth of the original SEG model ranges from 0 to 440 m. By increasing the seawater depth by 200 m, a 200-m-long vertical electric-dipole source can be placed anywhere above the seafloor. When the change is made, the seawater depth varies from 220 to 380 m along the survey line (Figure 1c).

Second, we introduce into the offshore model a cylindrical hydrocarbon reservoir whose radius and thickness are 2500 m and 100 m, respectively. The center of the reservoir is placed at  $x = 4500$  m,  $y = 0$  m,  $z = 950$  m. The reservoir does not intersect the salt dome, but is slightly above it. The reservoir is also tilted by  $5^\circ$  toward the negative  $x$ -direction. In our modeling, the resistivities of the seawater, the seabed, the reservoir, and the salt dome are set to 0.3, 0.7, 100, and 100  $\Omega\text{m}$ , respectively. Figure 2 shows the cross-sectional view of the offshore model along the survey line.

As discussed in Um et al. (2010), the external boundaries of an FE model should be sufficiently far from the source location to eliminate unwanted boundary effects at receiver locations. To ensure this is the case, we first extend the seafloor topography along the boundaries of the model an additional 15 km in the  $x$ - and  $y$ -directions, respectively. Then, we insert the offshore model into a much larger layered-background offshore model that measures 500 km in each direction. The layered background offshore model consists of the air, the seawater, and the seabed. Their thicknesses are 250 km, 500 m, and 249.5 km, respectively.

We construct nine different FETD meshes for the offshore model (Figure 1). Each mesh includes one source location and eleven receiver locations. On average, the mesh consists of 412,786 tetrahedral elements, resulting in 480,868 unknowns. The average solution

time for the mesh is about four hours on a 2.26 GHz Intel Nehalem single core using 20 GB memory. During the simulations above, the step-off source waveform has been employed. When necessary, impulse responses to the models are approximated by taking time-derivatives of step-off responses. This indirect computation helps us reduce modeling costs because the direct use of an impulse waveform requires finer mesh around a source and a smaller initial time-step size than a step-off waveform.

To ensure the accuracy of the FETD mesh, the solutions should be compared to solutions obtained using other methods. First, to compare the FETD solutions with analytical solutions (K. H. Lee, personal communication, 2007), the resistivities of the seabed, the reservoir, and the salt dome in the FETD meshes are set to that of the seawater. Then, we compute the FETD and analytical solutions for the half-space seawater model and compare them each other. We continue to refine the FETD meshes until the two solutions agree to within 3%. Next, the resistivity of the lower half-space in the FETD mesh is set to a new value (e.g., the resistivity of the seabed). The comparison procedures above are repeated. Note that this approach does not absolutely guarantee that the constructed FETD meshes produce accurate solutions because large resistivity contrasts between the seabed, the reservoir, and the salt dome are not considered. However, this approach allows us, with relatively low computational cost, to quickly check whether the FETD mesh is approximately correct.

Second, the resistivities of the seabed, the reservoir, and the salt dome are reset to the original values mentioned before. Then, we compute 3D FETD solutions using two different FETD algorithms; one is based on the electric-field diffusion equation (Um et al., 2010), and the other on a potential diffusion equation (Um, 2011). When the two FETD algorithms share the same mesh, the comparison between the two FETD solutions can be used to measure the mesh quality. By checking the mesh quality through these two verification procedures, we ensure that the two FETD solutions show less than 3% differences and assume that they are accurate enough for the modeling analysis in the next sections. Figure 2 shows the cross-sectional view of a central portion of the FETD meshes along the survey line (i.e.,  $y = 5$  km). The meshes illustrate typical characteristics of spatial discretization for time-domain EM diffusion problems: elements are smallest near the source and the receivers and gradually go away from them. Beyond the central portion of the computational domain, elements increase using a growth factor which is empirically determined but usually smaller than a factor of two from one edge to another. The reader is referred to Um et al. (2010) for more examples about FETD mesh design.

### ANALYSIS OF ELECTRIC FIELD DIFFUSION IN OFFSHORE MODELS

To understand CSEM responses to the complex offshore models described above, we successively consider four offshore seabed scenarios with increasing geometric complexity: (1) an offshore model without the reservoir and the salt dome, (2) an offshore model that includes only the reservoir, (3) an offshore model that includes only the salt dome, and (4) an offshore model that includes both the reservoir and the salt dome. For the sake of convenience, these four seabed scenarios are called “the background model,” “the reservoir model,” “the salt model,” and “the reservoir-and-salt model,” respectively. For a given source location, these four different seabed scenarios can be simulated using a single FE mesh. Before

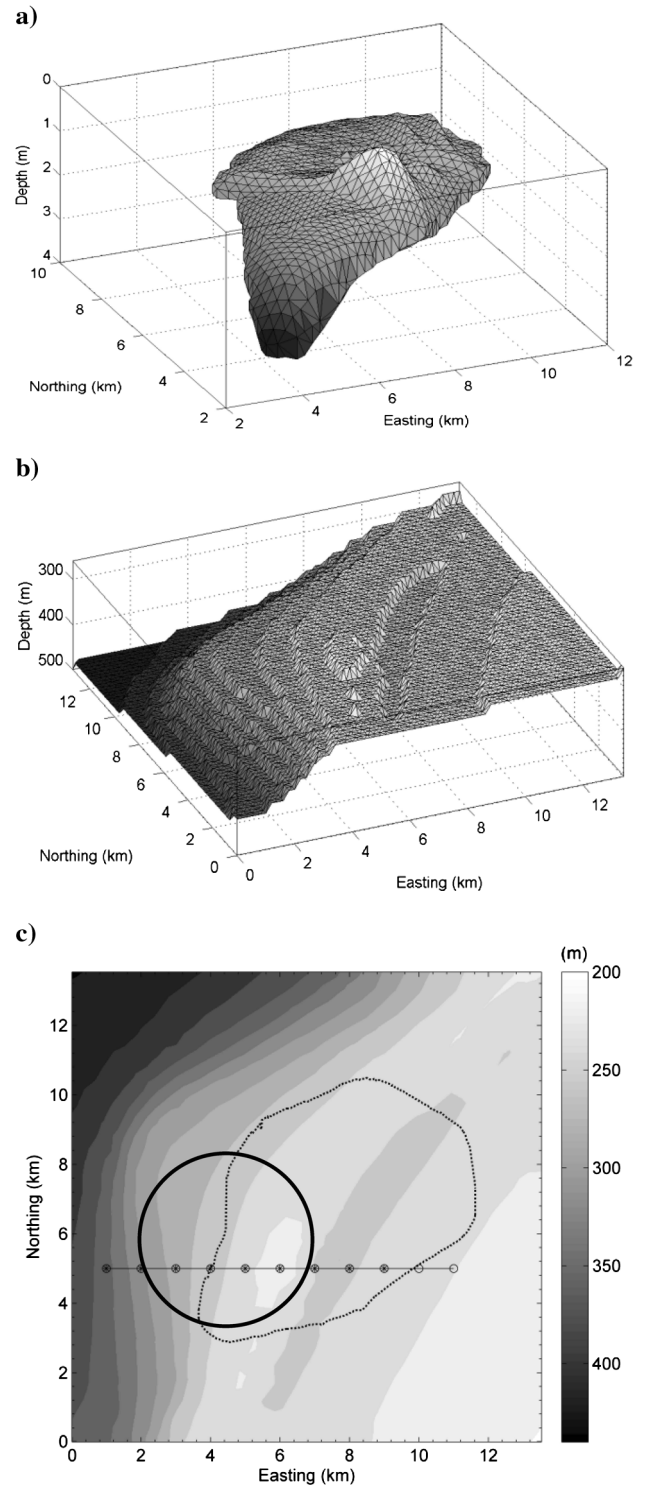


Figure 1. The 3D offshore model that is modified from the SEG salt model. The reconstructed 3D surfaces of (a) the salt and (b) the seafloor. (c) The topography map with the survey line. In (c), the solid line indicates the boundary of the hydrocarbon reservoir, and the broken line the boundary of the reconstructed SEG salt body. The asterisks and circles represent the source and receiver positions, respectively.

we compare the short-offset electric-field measurements from the four models along the survey line, we first examine cross sectional animations of the transient electric fields for each model (Figures 3, 4, 5, and 6). Although nine VED source positions are considered along the survey line, we primarily focus on a VED source at  $x = 3$  km in this section because its electric fields interact well with both the reservoir and the salt dome and produce strong anomalous electric fields.

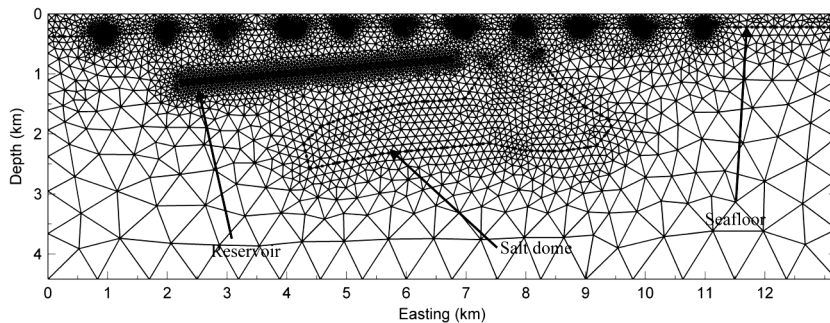


Figure 2. A cross-sectional view of a central portion of FETD meshes along  $y = 5$  km (along the survey line shown in Figure 1c). In this sample mesh, the source is placed on the seafloor at  $x = 3$  km. Ten receivers are placed with 1 km interval on the seafloor.

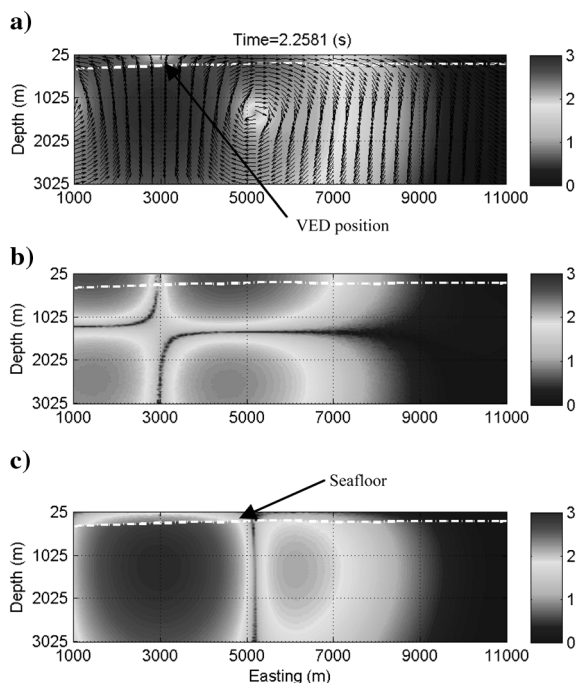


Figure 3. A snapshot of the animation showing the transient electric fields in the background model. (a) The total electric fields. (b) The horizontal electric fields. (c) The vertical electric fields. The full-color animation file, [animation3.mov](#), is linked to the black and white snapshot above. In the animation, the black arrows indicate the directions of the electric fields. The green line segment indicates the VED. The white broken line represents the seafloor. The color bar represents the amplitude of the electric fields normalized by its maximum on the cross-section. To better render the variation of the electric fields on the cross section, the minimum and maximum electric fields are scaled to 0 and 3, respectively, on a common log scale.

First, we examine the diffusion of the transient electric fields for the background model (Figure 3). When the source is excited, the electric fields quickly become horizontal in the thin water column due to the air-seawater interface. The maximum of the electric fields does not remain close to the source position over time, but diffuses outward from the source position. This maximum of the high concentration does not contain the information about the seabed, but is merely the direct diffusion of the electric fields from the source through the seawater. Thus, when the seafloor electric fields are measured at short offsets, the measurements would be affected by the direct diffusion only in early time, but not in late time where the short-offset configuration is sensitive to a deep resistive target (Cuevas and Alumbaugh, 2011). Because the vortex of the electric fields diffuses obliquely downward over time, the vertical components of the seafloor electric fields  $E_z$  show sign reversals. The arrival time of the sign reversal depends on a source-receiver offset.

In the vicinity of the source, the distribution of the horizontal electric fields  $E_x$  is not always symmetric with respect to an imaginary vertical line that passes through the VED source (Figure 3b). As the electric fields continue to dif-

fuse, the narrow zone free of the  $E_x$  is shifted toward the left of the source. As a result, in the vicinity of the source,  $E_x$  receivers (e.g.,  $x = 2$  km) can record a sign reversal in the late time. In fact, the sign reversal is the direct result from the irregular seafloor topography because the spatial distribution of the  $E_x$  is symmetric with respect to a source in a layered offshore model. Note that along the survey line, the slope of the topography does not exceed  $2^\circ$ . Thus, Figure 3 demonstrates that short-offset  $E_x$  measurements are extremely sensitive to the multidimensional nature of seafloor topography. In the next section, we will further examine a mechanism of the sign reversal and its implication.

Next, the reservoir is inserted into the background model, and we examine its effects (Figure 4). As the transient electric fields diffusing directly below the source are blocked by the reservoir, the high concentration of the electric fields is normally incident upon the seabed-reservoir interface. The strong electric fields develop inside the reservoir due to the continuity of the normal current density. The electric fields inside the reservoir remain normal to the interface over time, resulting in the galvanic effects. Short-offset measurements will record the perturbation in the electric fields. The electric fields also diffuse faster through the resistive reservoir than the conductive background seabed, and the degree of attenuation through the reservoir is insignificant compared with that through the conductive seabed. Figure 4 illustrates the development of a guided mode (Weidelt, 2007) in the thin resistive reservoir.

Next, the reservoir is replaced with the salt dome (Figure 5). In this case, the source is not directly above the salt dome. Therefore, the high concentration of the electric fields emanating from the lower tip of the source continues to diffuse downward below the source. Although the high concentration of the electric fields diffuses into the elongated part of the salt dome later. This phenomenon does not affect the electric field distribution in the vicinity of the source. Therefore, short-offset measurements would not clearly detect the presence of the salt dome. Figure 5 implies that the short offset

configuration would be a useful mapping tool for lateral boundaries of a structure directly below a VED source. Its effectiveness will be discussed in the next section where the short-offset seafloor-electric-fields measurements are examined at multiple source positions along the survey line.

Finally, we consider the reservoir-and-the-salt model (Figure 6). In the vicinity of the source, the evolution of the transient electric fields is nearly identical to that in the reservoir model (Figure 4) over time. The complex interaction of the electric fields between the reservoir and the salt dome is observed later in depth, but the perturbation would not be measurable at short offsets. In the next section, we compare short-offset electric-field measurements of the four offshore models at multiple source positions and discuss their sensitivity to the reservoir, the salt dome, and the seafloor topography.

### SHORT-OFFSET TDCSEM MEASUREMENTS WITH VED SOURCE

Seafloor  $E_x$  and  $E_z$  measurements with 1 km offset along the survey line are presented in Figures 7 and 8, respectively. The short-offset measurements are simulated for 50 s because the late-time responses are sensitive to deep structures even at such short offsets (Cuevas and Alumbaugh, 2011). We assume that a receiver noise level is  $10^{-15}$  V/Am<sup>2</sup> (Um and Alumbaugh, 2007) and thus, the simulated measurements are above that level. First, we compare the background offshore model with the reservoir model. If there is no reservoir directly below the source, the two models produce approximately the same responses (Figure 7a and 7h; Figure 8a and 8h). However, as the source crosses the

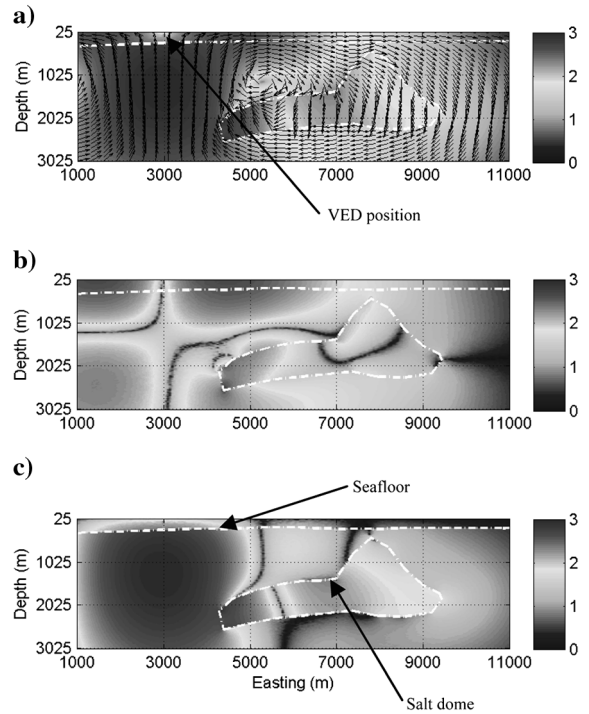


Figure 5. A snapshot of the animation showing the transient electric fields in the salt model. (a) The total electric fields. (b) The horizontal electric fields. (c) The vertical electric fields. The full-color animation file, [animation5.mov](#), is linked to the black and white snapshot above.

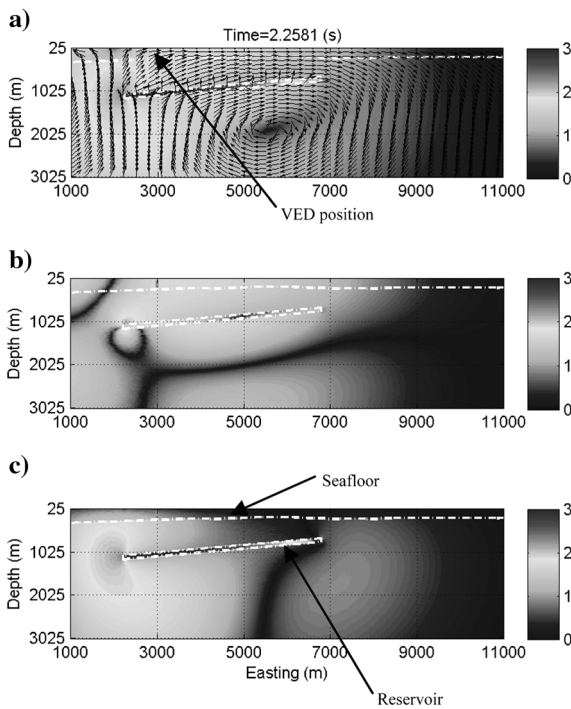


Figure 4. A snapshot of the animation showing the transient electric fields in the reservoir model. (a) The total electric fields. (b) The horizontal electric fields. (c) The vertical electric fields. The full-color animation file, [animation4.mov](#), is linked to the black and white snapshot above.

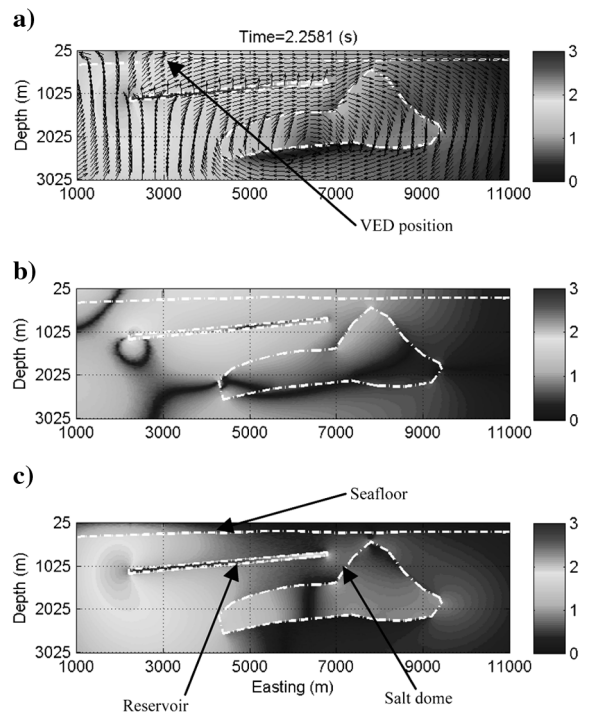


Figure 6. A snapshot of the animation showing the transient electric fields in the reservoir-and-salt model. (a) The total electric fields. (b) The horizontal electric fields. (c) The vertical electric fields. The full-color animation file, [animation6.mov](#), is linked to the black and white snapshot above.

reservoir, the reservoir responses start to deviate from the homogeneous seabed responses (Figure 7b–7g; Figure 8b–8g). The shallower the reservoir is, the earlier the deviation starts. It is also noteworthy that the  $E_z$  amplitudes from the background model can

be larger than those from the other three models that include the resistive structures.

Second, we extend the comparison to the salt model and the salt-and-reservoir model. The  $E_x$  and  $E_z$  measurements also sense the lateral extent and depth of the salt dome unless the salt dome is directly below the reservoir. In such a case, the reservoir effectively blocks the flow of the vertical electric fields toward the salt dome (Figure 6). The anomalous galvanic effects around the source (i.e., at short offsets) resulting from the salt dome become negligible. Therefore, the short-offset single-receiver measurements (Figure 7d and 7e; Figure 8d and 8e) become nearly blind to the salt dome directly below the reservoir.

Next, we examine the sensitivity and resolution of the short-offset electric-field measurements to the reservoir and the salt dome using a 1D inversion algorithm summarized in Appendix A. The 1D inversion algorithm utilizes a Newton-Gaussian method along with a cooling scheme for determining the regularization parameter (Farquharson and Oldenburg, 2004). Note that there are the limitations of inverting the 3D TDCSEM modeling data using the 1D inversion algorithm as will be demonstrated later. However, in this paper, we still consider the 1D inversion as our first-choice method, because unlike 3D marine FDCSEM inversion algorithms, 3D marine TDCSEM inversion algorithms are still in their infancy and are not yet readily available. High computational costs are also a major roadblock for their routine uses. Accordingly, 1D time-domain inversion over 3D structures has been conventional in time-domain EM interpretations until now (e.g., Auken et al., 2006; Árnason et al., 2010). Thus, as a part of this research, we will investigate the usefulness and the limitations of the 1D inversion approach to 3D TDCSEM modeling data, especially when source-receiver offsets are fairly short.

Before presenting the 1D inversion results, we first elucidate mechanisms of sign reversals observed in Figures 7 and 8. It is important to understand the mechanisms; if a sign reversal originates from the multidimensional nature of the offshore models, the 1D inversion would not work even at such short offsets. We first look at the  $E_z$  measurements (Figure 8). All  $E_z$  measurements show the sign reversals consistently at around 0.5 s. As mentioned, when the transient electric fields are analyzed on the cross-section of the background model (Figure 3), the sign reversals result from the vortex pattern of the electric fields that diffuses obliquely downward. Because the vortex pattern is not distorted by the deep structures (i.e., the reservoir and the salt dome) produce the sign reversal at the nearly same time.

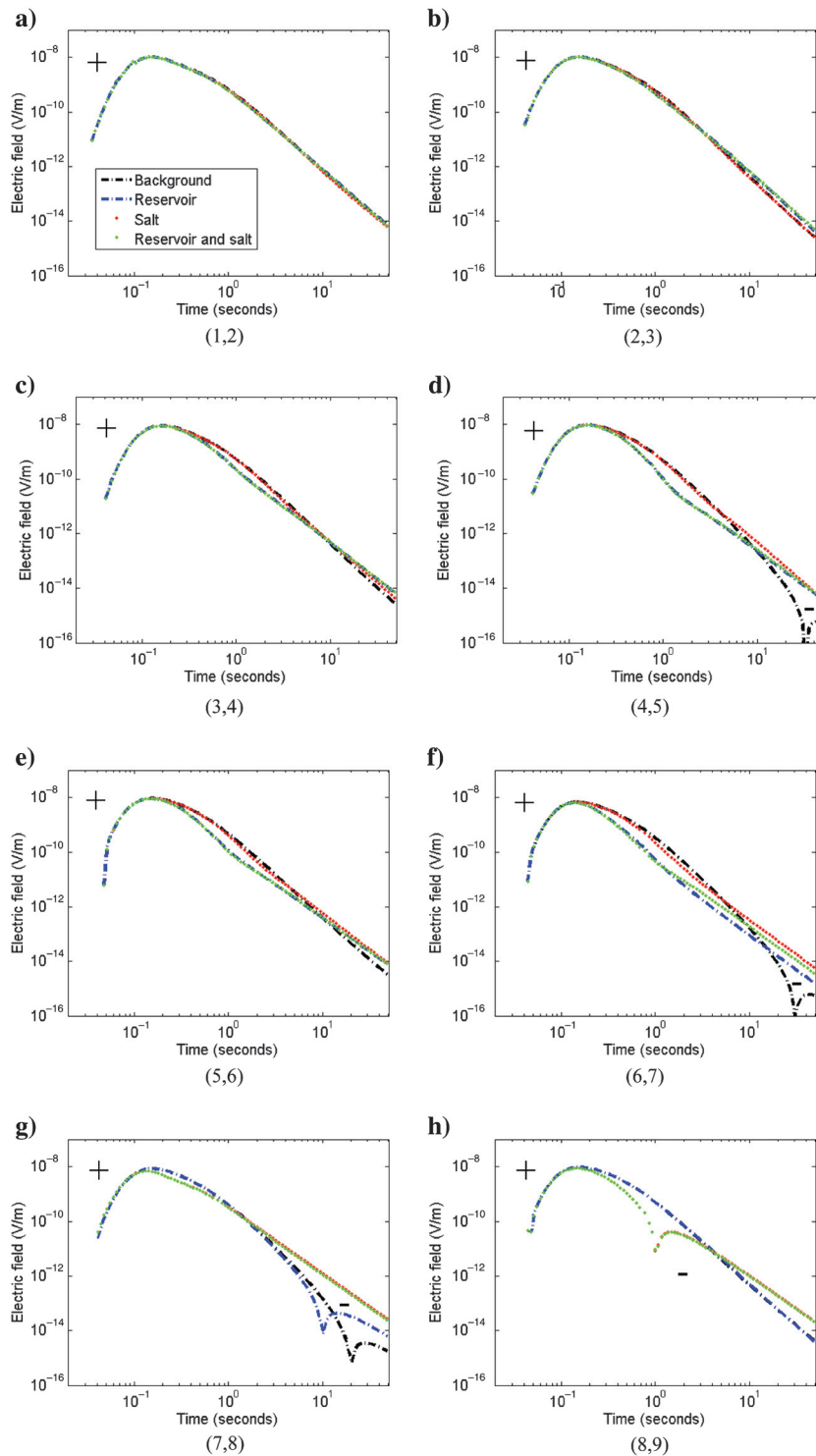


Figure 7. The 1-km-offset VED source- $E_x$  measurements over the four offshore models. In (a-h), the first and second number in the parentheses are the  $x$ -coordinate (km) of the VED source and the  $E_x$  receiver, respectively, along the survey line shown in Figure 1c.

In short, the sign reversal is not related to the 3D effects. In contrast, when the source and the receiver are placed at  $x = 7$  km and  $x = 8$  km, respectively, there is a complex salt dome top in the shallow depth (Figure 1). The shallow structure produces the anomalous sign reversals at around 2~3 seconds (Figure 8g). Therefore, the 1D inversion would not be applicable to the  $E_z$  measurements.

In contrast to the expected sign reversals of the  $E_z$  measurements discussed above, unusual sign reversals are observed in the  $E_x$  measurements at late times (Figure 7). For example, the background seabed model shows a sign reversal when a receiver is placed at  $x = 5, 7,$  and  $8$  km (Figure 7d, 7f, and 7g). Because a homogeneous flat seafloor model produces no sign reversal, it can be inferred that the sign reversal results from the subtle seafloor topography around the short-offset configuration. In fact, this sign reversal is the direct effect of the sloping seafloor around a VED source. To illustrate the effect, we consider a simple 2D sloping seafloor model (Figure 9). As shown in Figure 9a, the VED source is not normal to the seafloor due to the sloping seafloor. Therefore, Figure 9a can be rotated clockwise by the angle of the slope such that the seafloor becomes flat, but the VED source is tilted instead (Figure 9b). The tilted VED source can be decomposed into the VED' and HED' sources. Accordingly, the constructive and destructive interaction of the VED' and HED' sources can explain the sign reversal at a short offset.

For example, sometime after the VED' source is excited, the  $E_x$  direction in the left and right side of the VED' source are negative and positive, respectively (Figure 9c). In contrast, when the HED' source is excited, the  $E_x$  direction on both the left and right sides of the HED' source is positive (Figure 9d). As a result, the sign reversal of  $E_x$  measurements can be observed in the left side of the VED source (i.e., toward the sloping direction). As shown in Figure 7, the sign reversal usually occurs at late times. To explain this, we compare the electric field diffusion pattern of the background offshore model excited by a VED source (Figure 3) with that by an HED source (Figure 10). The  $E_x$  maximum of the VED' source diffuses outward from the source position over time. In contrast, the  $E_x$  maximum of the HED' source remains close to the source position over time. Therefore, although a gently sloping seafloor (e.g., 2°) produces a large VED' source and a small HED' source, the  $E_x$  field of the HED' source can exceed that of VED' source at a short offset at late time. Consequently, the sign reversal occurs. In addition to this conceptual approach to understanding the mechanism of the sign reversal,

we further demonstrate the sensitivity of the two short-offset configurations to a 2D sloping seafloor as a function of a slope angle in Appendix B.

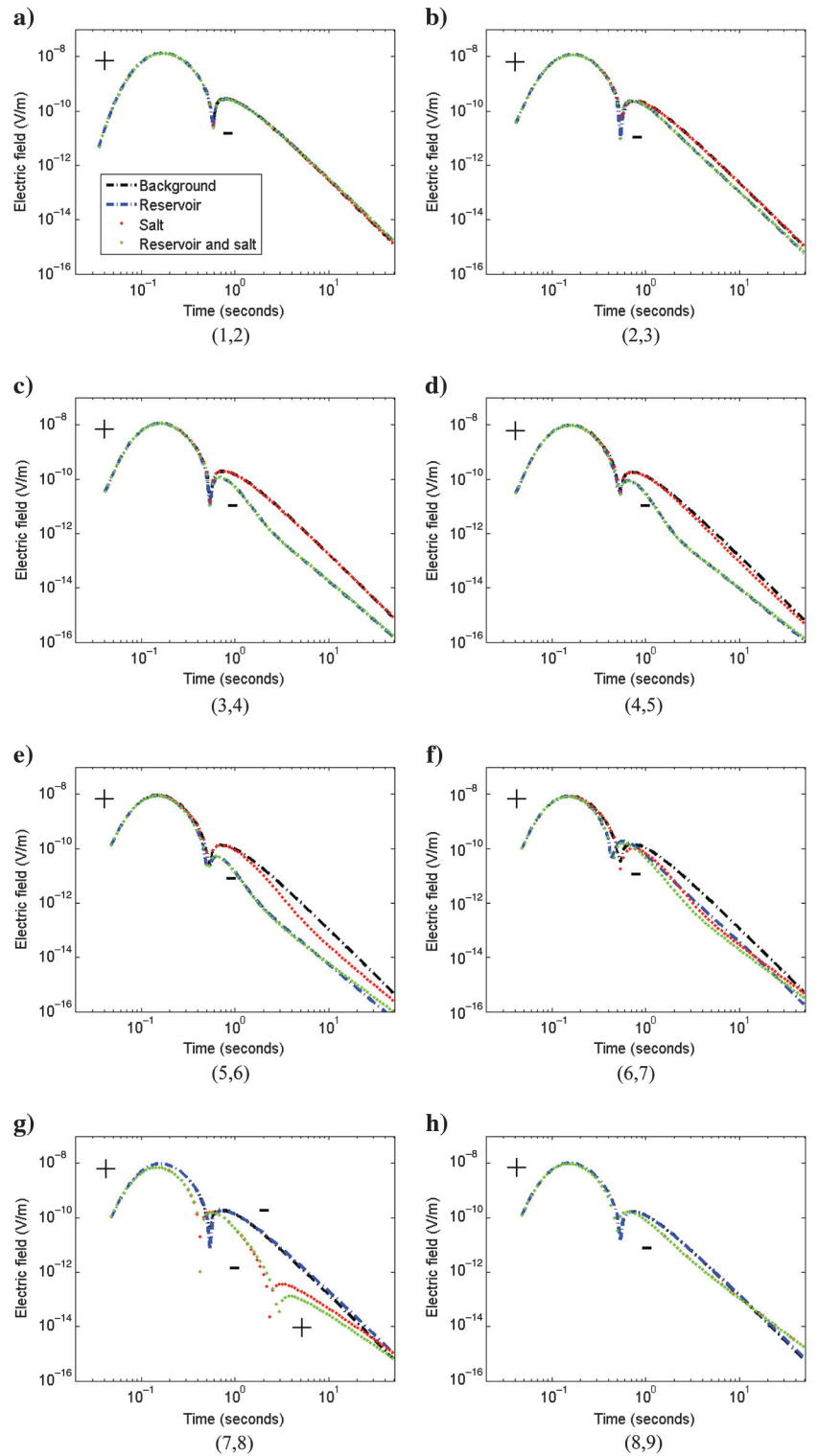


Figure 8. The 1 km-offset VED source- $E_z$  measurements over the four offshore models. In (a-h), the first and second number in the parentheses are the  $x$ -coordinate (km) of the VED source and the  $E_z$  receiver, respectively.

Figure 11 shows 1-km-offset  $E_x$  and  $E_z$  measurements over the background offshore model along the survey line (Figure 1c). For each source, the  $E_x$  and  $E_z$  measurements are plotted at two receiver locations. One receiver is 1-km from a given VED source in the left

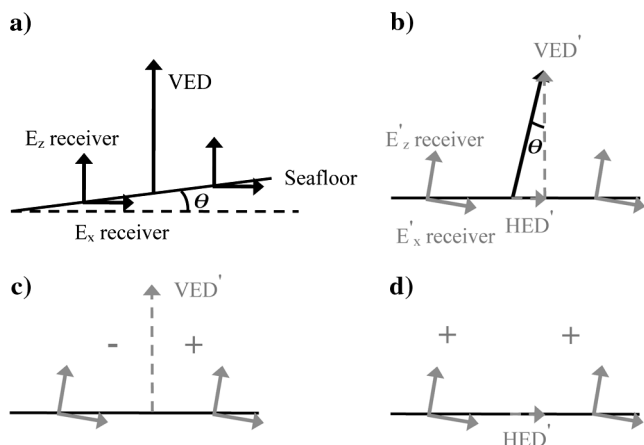


Figure 9. The geometric analysis of the VED source on the 2D sloping seafloor. (a) The VED source on the 2D sloping seafloor. The arrow of the VED source indicates the source polarization;  $\theta$  is the slope angle. (b) The clockwise rotation of Figure 9a by  $\theta$ . The VED source is decomposed into the  $VED'$  and  $HED'$  sources. (c) The  $VED'$  source on the flat seafloor; - and + indicate the  $E_x$  direction in the left and right sides of the  $VED'$  source. (d) The  $HED'$  source on the flat seafloor.

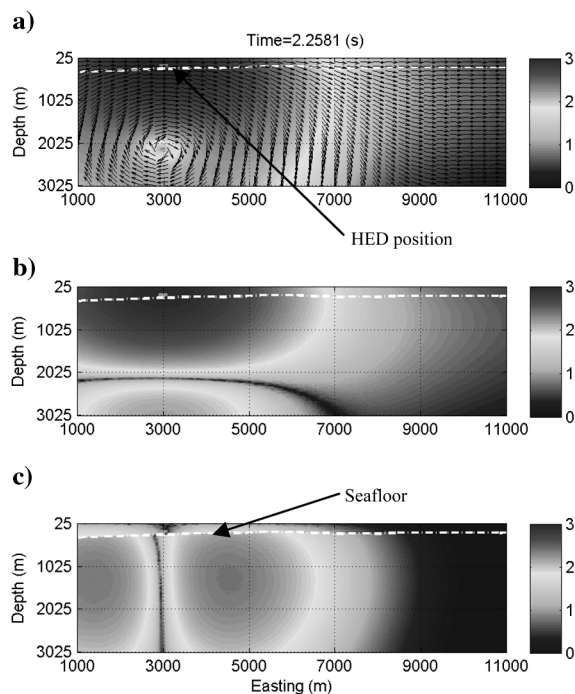


Figure 10. A snapshot of the animation showing the transient electric fields in the background model. A 200 m long HED source is placed at  $x = 3$  km. (a) The total electric fields. (b) The horizontal electric fields. (c) The vertical electric fields. The full-color animation file, [animation10.mov](#), is linked to the black and white snapshot above.

direction (negative  $x$ -direction). The other one is 1-km from the VED source in the right direction (positive  $x$ -direction). Table 1 shows the average slope angle at each VED position and its direction. By comparing Figure 11 with Table 1, one can confirm that the  $E_x$  measurements consistently show a sign reversal in the sloping direction. In contrast, the  $E_z$  measurements are robust to the subtle change of the seafloor topography.

The analysis above illustrates that the  $E_x$  measurements are very sensitive to the multidimensional nature of the seafloor topography. Therefore, unless the subtle seafloor topography is measured and modeled very accurately, the  $E_x$  measurements would be prone to measurement and modeling errors at short offsets. We also conclude that the 1D inversion is not applicable to the  $E_x$  measurements due to their sensitivity to the subtle seafloor topography even at the short offset. In contrast, the  $E_z$  measurements are less sensitive to a subtle change of the seafloor topography as shown in Figure 11 and can be considered a practical choice for the 1D inversion. In the next section, using the 1D inversion, we attempt to invert the  $E_z$  measurements and discuss the vertical and lateral resolution of the measurements to the reservoir and the salt dome.

## 1D INVERSION ANALYSIS

For the 1D inversion, we assume that the 3D FETD modeling data (i.e., the short-offset measurements) have less than 3% numerical errors due to spatial discretization and time-stepping processes. The 1D inversion algorithm is designed for a user to add extra noises (e.g., 5% of amplitudes) to the data. However, in this inversion analysis, we do not add such extra noises to the FETD modeling data because the goal of the analysis is to examine, not the effect of the noise level on the 1D inversion, but the sensitivity of the short-offset measurements. A starting model is prepared at each source position. The starting model is simply a homogeneous seabed model. Its seawater depth is set to that of the 3D offshore models at a given source position and is fixed during the inversion. Therefore, a receiver that is 1 km off from the source might not be placed exactly on the seafloor if the seafloor of the 3D offshore model is not flat between the source and the receiver. Instead, the receiver can be placed either slightly above or below the seafloor. As shown below, this discrepancy introduces topography effects into the 1D inversion when the short-offset responses to the 3D background offshore model are inverted. The resistivities of the seawater and the seabed in the starting model are also the same as those in the 3D background offshore model.

Figure 12 shows the comparison between the  $E_z$  measurements from the 3D seabed models and those from the final layered seabed models (Figure 13) determined by the 1D inversion. As shown in Figure 12g, it failed to invert the  $E_z$  measurements over the salt model and the reservoir-and-salt model when the source was placed at  $x = 7$  km. In this case, the 1D inversion does not work properly due to strong 3D effects resulting from the shallow salt dome top below the source. Except for this source position, the 1D- and 3D-modeled  $E_z$  measurements agree well (Figure 12). Figure 13 includes the 1D inversion result of the 3D background offshore model. The deviation of the inversion of the 3D background offshore model from 0.7  $\Omega\text{m}$  half-space can be considered the effect of the 3D bathymetry. Although the deviation is observed from Figure 13a–13i, the degree of the deviation is reasonably small, indicating that the short-offset VED- $E_z$  configuration is robust to the subtle topography change.

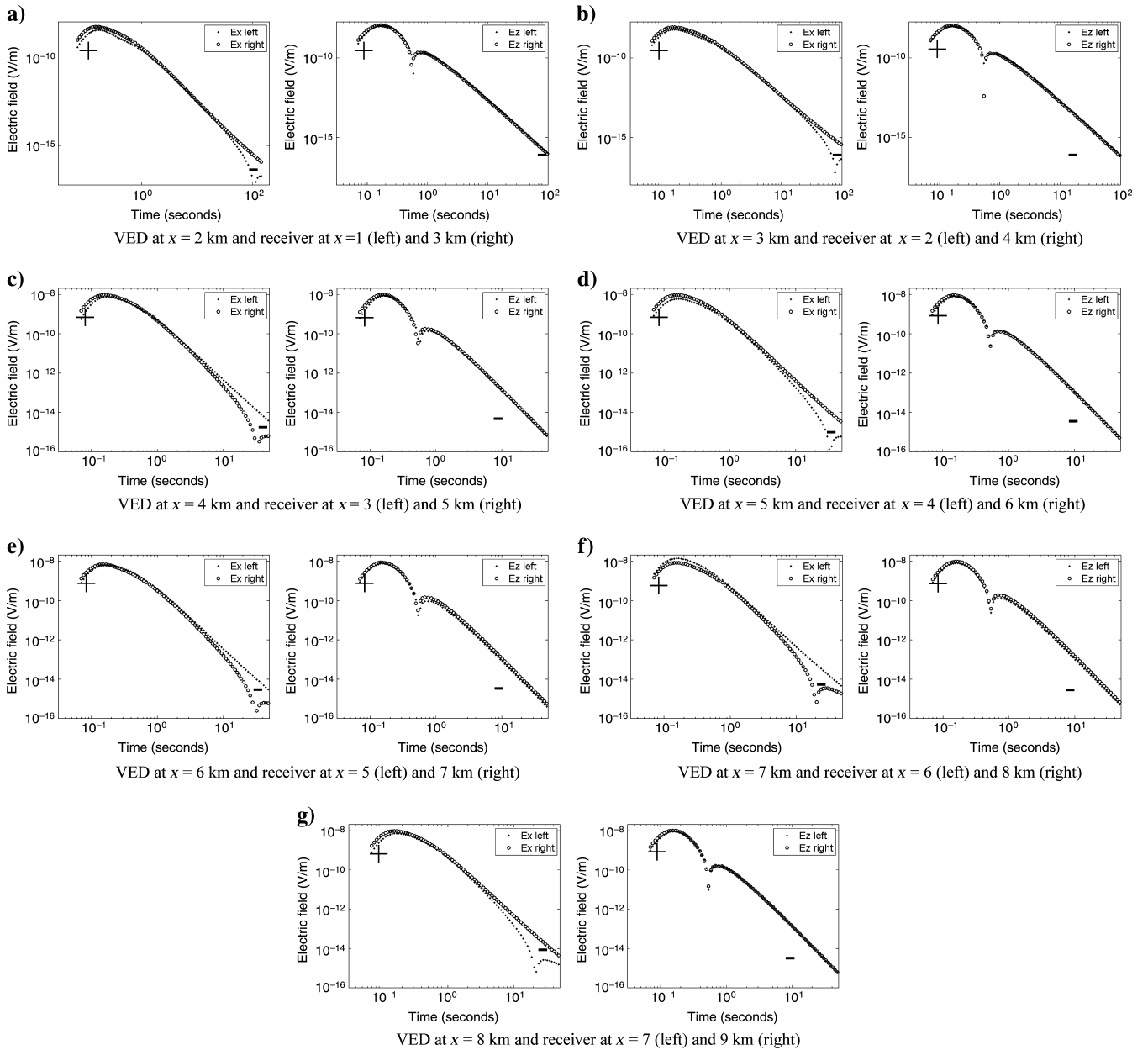


Figure 11. The comparison of the  $E_x$  and  $E_z$  measurements over the background offshore model. The  $E_x$  and  $E_z$  components are plotted at two receivers that are 1 km from each VED source in the left and right direction along the survey line.

**Table 1.** The average slope angle and the direction at each VED source position along the survey line (Figure 1c). The left and right directions indicate the negative and positive  $x$ -direction along the survey line.

VED	2 km	3 km	4 km	5 km	6 km	7 km	8 km
Slope angle (direction)	$-2^\circ$ (left)	$-2^\circ$ (left)	$+1^\circ$ (right)	$-2^\circ$ (left)	$+2^\circ$ (right)	$+2^\circ$ (right)	$-2^\circ$ (left)

The inversion results show that the short-offset  $E_z$  measurements do not have sufficient resolution of the reservoir and the salt dome. The true thickness and resistivity of the structures are significantly smeared out. Neither does the depth of the peak resistivity of the recovered reservoir agree with the true depth (Figure 13c, 13d, 13e, and 13f). This result agrees with analytic studies of short-offset measurements in “infinitely” deep water environments (Alumbaugh et al., 2010; Cuevas and Alumbaugh, 2011); near a VED source, the electric field responses are mainly described by the superposition of image sources associated with charge buildups on a resistor and lack the guided mode that is primarily measured in the long-offset

regime and provides the enhanced resolution. In short, without the guided mode, the short-offset measurements result in poor resolution. As can be expected from the previous forward modeling analysis, when a source and a receiver are placed at the center of the reservoir (Figure 13d and 13e), the reservoir model and the reservoir-and-salt model produce a nearly identical resistivity structure, reconfirming that the short-offset measurements are mainly sensitive to the uppermost resistor.

However, despite the limitations, the short-offset single-receiver inversion also reveals some encouraging results. Although the starting depths of the reservoir and the salt dome are not recovered

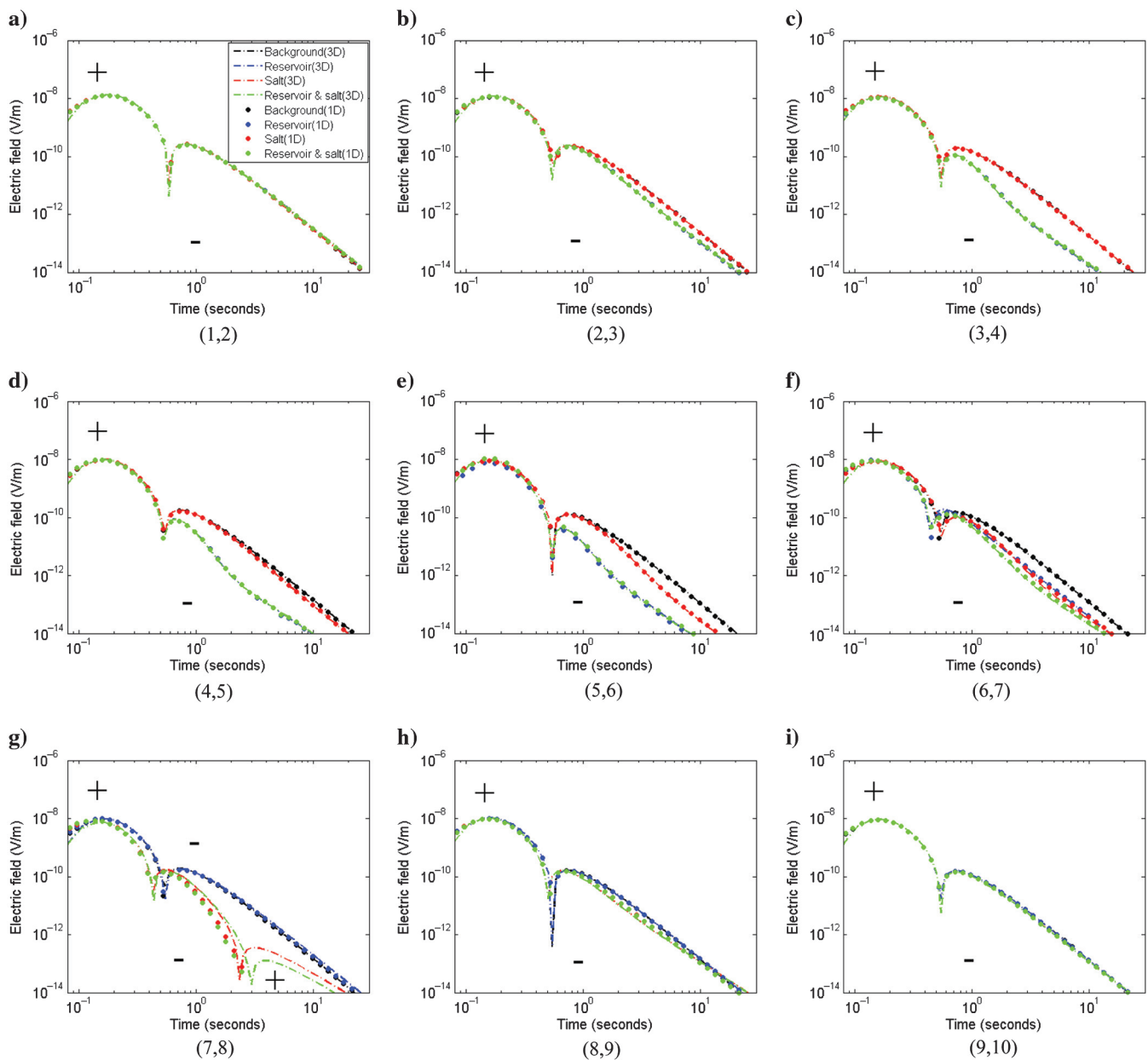


Figure 12. Comparison of the short-offset  $E_z$  measurements from the 3D FETD models and the layered seabed models (Figure 13) resulting from the 1D inversion. In (a-i), the first and second number in the parentheses are the  $x$ -coordinate (km) of the VED source and the  $E_z$  receiver, respectively, along the survey line.

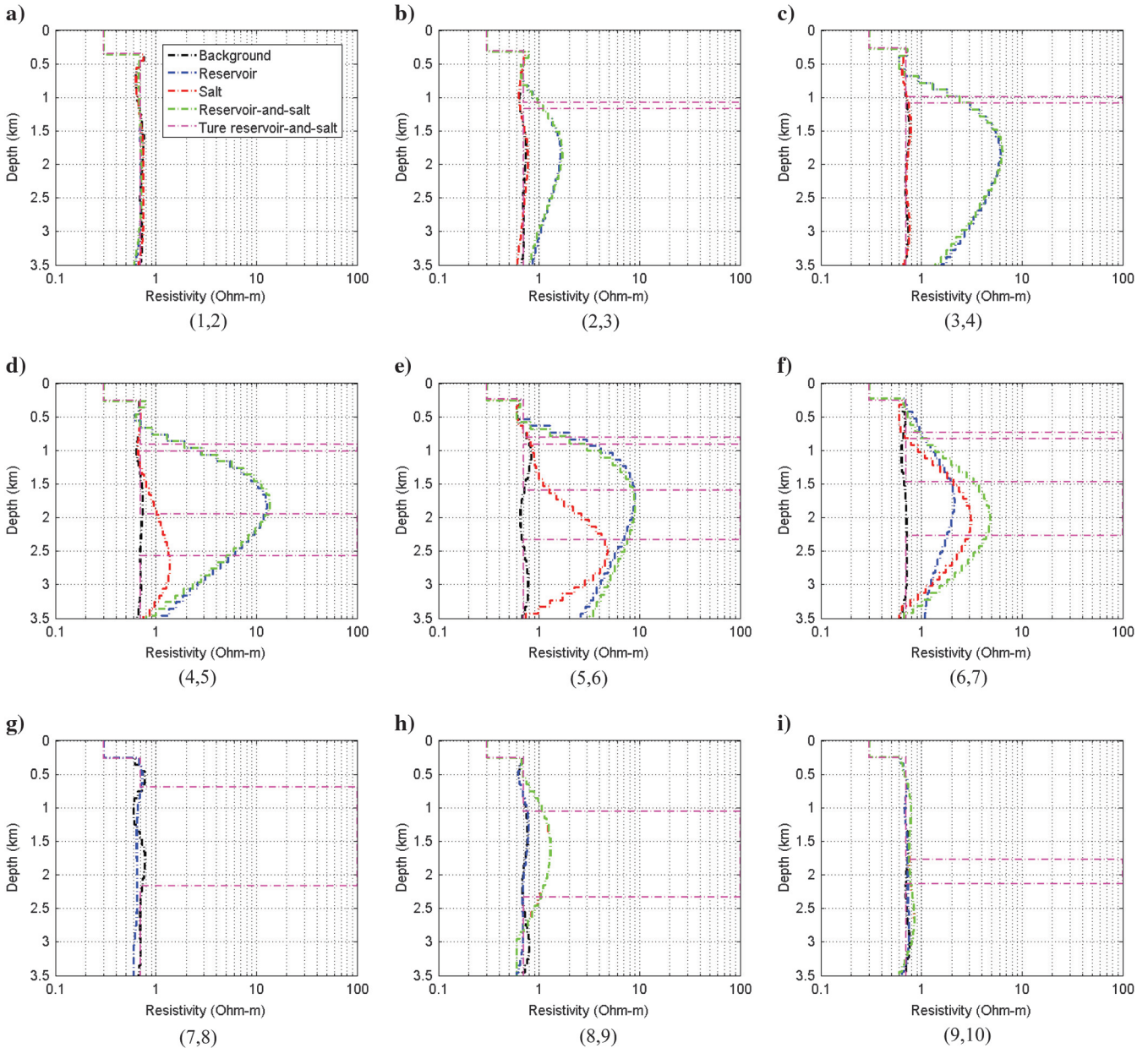


Figure 13. Seabed resistivity structures obtained from 1D inversion of the  $E_z$  measurements over the four offshore models along the survey line. In (g), the  $E_z$  measurements of the salt model and the salt-and-reservoir models were not successfully inverted by the 1D algorithm due to their strong 3D nature and were excluded from here. The true reservoir-and-salt model is also plotted as a reference model. The true model is defined as the 1D resistivity structure of the 3D reservoir and salt model at the midpoint between source and receiver.

accurately, the inversion results indicate that the salt dome is a deeper structure than the reservoir (Figure 13d, 13e, and 13f). More importantly, the measurements and their inversion are sensitive to the lateral extent of the reservoir and the salt dome. For example, the lateral extent of the reservoir from the inversion results is bound between  $x = 2$  km and  $x = 7$  km (Figure 13b–13f). This result agrees with the true lateral extent of the reservoir (Figure 1). The inversion result showing that the salt dome lies from  $x = 4$  to 9 km also agrees with its true geometry. In short, we conclude that, although the short-offset measurements fail to recover its true thickness and

resistivity, they can still provide useful insights into the lateral extent and depth of the localized reservoir and the salt dome.

### CONCLUSIONS

Through 3D FETD modeling studies, we have analyzed the sensitivity of short-offset electric-field measurements excited by a VED source to the irregular seafloor topography, the localized reservoir, and the large-scale salt dome. FETD simulation and visualization approaches play important roles in understanding overall characteristics of the electric field diffusion related to the

sensitivity of the short-offset measurements. The modeling analysis indicates that the short-offset measurements effectively sense the presence of the reservoir and the salt dome if they are placed directly below the source.

Although a short source-receiver offset (i.e., 1 km) is employed and the slope of the seafloor along the survey line does not exceed  $2^\circ$ , the numerical modeling studies show that the subtle seafloor topography near the source does influence the  $E_x$  measurements and results in sign reversals at late times. The sign reversal directly results from the VED source no longer being normal to the seafloor. This aspect would limit the application of the short-offset  $E_x$  measurements in practice unless the subtle change of the seafloor topography is accurately measured near the source and is taken into account during numerical modeling.

In contrast, the short-offset  $E_z$  measurements are robust to the subtle changes of seafloor topography near the source. Thus, it is possible to invert the short-offset  $E_z$  measurements with the 1D algorithm. Although we successfully applied the 1D inversion to the most  $E_z$  measurements, the 1D inversion did not work around a source/receiver position where there exists strong multidimensional geology in a shallow depth. The inversion results suggest that the short-offset  $E_z$  measurements lack the resolution of the reservoir and the salt dome in terms of the thickness and the resistivity, but do detect their lateral extent fairly well.

## ACKNOWLEDGMENTS

We express our gratitude to Schlumberger-EMI Technology Center for the permission to use its 1D inversion code. Additionally, E. U. is partially supported by Chevron Stanford Graduate Fellowships in Science and Engineering.

## APPENDIX A

### 1D TIME-DOMAIN INVERSION ALGORITHM

A forward modeling engine in the 1D time-domain inversion algorithm has been developed based upon the frequency-domain 1D modeling code EM1D (K. H. Lee, personal communication, 2007). The time-domain responses are inverse Fourier-transformed from its counterpart in frequency-domain, which is sampled in logarithmic frequency, spline interpolated, and then convolved with a transmitter current waveform. In the 1D inversion, the 1D model is uniformly divided into a large number of layers, each of which has a constant resistivity. The thicknesses of layers are fixed, and the logarithm of resistivity is the inversion parameter.

Following Farquharson and Oldenburg (2004), a time-domain inverse problem is solved by minimizing an objective function of the form

$$\Phi(m) = \phi_d(m) + \beta\phi_m(m), \quad (\text{A-1})$$

where the data misfit term is given as

$$\phi_d(m) = \|\mathbf{W}_d(d^{\text{pred}} - d^{\text{obs}})\|^2 \quad (\text{A-2})$$

and the model norm term is given as

$$\phi_m(m) = \|\mathbf{W}_m(m - m_0)\|^2. \quad (\text{A-3})$$

The quantity  $m$  is the model parameter ( $\log(\rho)$ );  $m_0$  is the reference model;  $\phi_d$  is a measure of data misfit;  $\phi_m$  is a measure of some property of the earth model;  $\beta$  is the regularization parameter;  $\mathbf{W}_m$  is the model weighting matrix derived from the minimum structure specification;  $\mathbf{W}_d$  is the weighting matrix for the “observed” time-domain data  $d^{\text{obs}}$ , and its diagonal element was the inverse estimated standard deviation of the data noise, plus a noise threshold was added;  $d^{\text{pred}}$  is the predicted data computed for the current resistivity model.

A standard Gauss-Newton approach is used. The regularization parameter  $\beta$  is determined at each iteration from a cooling scheme. The initial  $\beta$  is a trade-off between the initial data misfit and the model norm terms and is set large enough, and then is reduced by a constant factor, ranging from 1.5 to 2, at each of the following iterations. The Jacobian matrix is calculated using the brute-force finite difference method for simplicity. The perturbation of the model parameter at each iteration is obtained by solving the resulting normal equation using the singular-value decomposition method (Golub and Van Loan, 1996). The step length is determined from the polynomial line search (Kelley, 1999). Then the model  $m$  is updated until a convergence criterion is satisfied.

## APPENDIX B

### SENSITIVITY OF SHORT-OFFSET E-FIELD MEASUREMENTS TO SLOPE ANGLE

The sign reversal at a short offset discussed in the main text can be easily identified using analytic solutions (K. H. Lee, personal communication, 2007) and coordinate transformations. For example, consider a whole space earth model that consists of lower half-space homogeneous seabed and upper half-space seawater. A vertical electric dipole source is tilted by  $\theta$  degrees as shown in Figure 9b. One can analytically compute short-offset electric field responses to this configuration and then obtain the short-offset electric field responses to the sloping seafloor (Figure 9a) by 2D coordinate transformation. The tilting angle of the vertical dipole source corresponds to a seafloor sloping angle. In this case, the effect of the air-seawater interface is not considered, but one can demonstrate the sensitivity of short-offset  $E_x$  and  $E_z$  measurements to the subtle seafloor slope angles (Figure B).

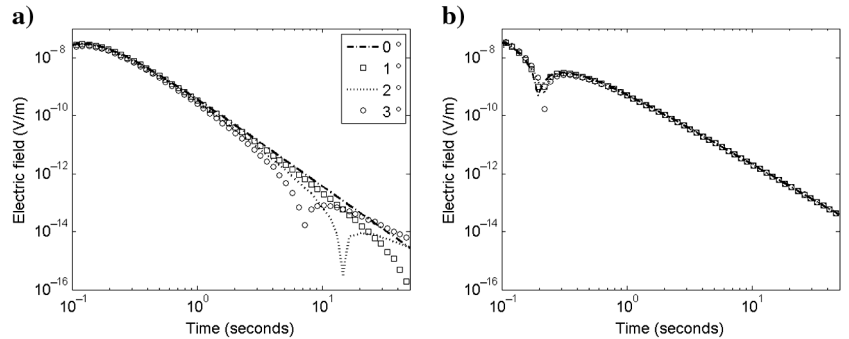


Figure B. (a)  $E_x$  and (b)  $E_z$  as a function of a seafloor slope angle ranging from  $0^\circ$  to  $3^\circ$ . Source-receiver offset is set to 500 m.

## REFERENCES

- Abubakar, A., T. Habashy, V. Druskin, L. Knizhnerman, and D. Alumbaugh, 2008, 2.5D forward and inverse modeling for interpreting low-frequency electromagnetic measurements: *Geophysics*, **73**, no. 4, F165–F177, doi: [10.1190/1.2937466](https://doi.org/10.1190/1.2937466).
- Alumbaugh, D., N. Cuevas, J. Chen, G. Gao, and J. Brady, 2010, Comparison of sensitivity and resolution with two marine CSEM exploration methods: 80th Annual International Meeting, SEG, Expanded Abstracts, 3893–3897.
- Aminzadeh, F., J. Brac, and T. Kunz, 1997, 3D salt and overthrust models: SEG/EAGE.
- Árnason, Knútur, Hjálmar Eysteinnsson, and Gylfi Páll Hersir, 2010, Joint 1D inversion of TEM and MT data and 3D inversion of MT data in the Hengill area, SW Iceland: *Geothermics*, **39**, 13–34, doi: [10.1016/j.geothermics.2010.01.002](https://doi.org/10.1016/j.geothermics.2010.01.002).
- Auken, Esben, Louise Pellerin, Niels B. Christensen, and Kurt Sørensen, 2006, A survey of current trends in near-surface electrical and electromagnetic methods: *Geophysics*, **71**, no. 5, G249–G260, doi: [10.1190/1.2335575](https://doi.org/10.1190/1.2335575).
- Barber, C. B., D. P. Dobkin, and H. T. Huhdanpaa, 1996, The Quickhull algorithm for convex hulls: Association for Computing Machinery. Transactions on Mathematical Software, **22**, 469–483, doi: [10.1145/235815.235821](https://doi.org/10.1145/235815.235821).
- Chave, A., 2009, On the electromagnetic fields produced by marine frequency domain controlled sources: *Geophysical Journal International*, **179**, 1429–1457, doi: [10.1111/gji.2009.179.issue-3](https://doi.org/10.1111/gji.2009.179.issue-3).
- Cheesman, S., R. Edwards, and A. Chave, 1987, On the theory of sea-floor conductivity mapping using transient electromagnetic systems: *Geophysics*, **52**, 204–217, doi: [10.1190/1.1442296](https://doi.org/10.1190/1.1442296).
- Chen, J., and D. Alumbaugh, 2011, Three methods for mitigating airwaves in shallow water marine controlled-source electromagnetic data: *Geophysics*, **76**, no. 2, F89–F99, doi: [10.1190/1.3536641](https://doi.org/10.1190/1.3536641).
- Commer, M., and G. Newman, 2008, New advances in three-dimensional controlled-source electromagnetic inversion: *Geophysical Journal International*, **172**, 513–535, doi: [10.1111/gji.2008.172.issue-2](https://doi.org/10.1111/gji.2008.172.issue-2).
- Cuevas, N., and D. Alumbaugh, 2011, Near-source response of a resistive layer to a vertical or horizontal electric dipole excitation: *Geophysics*, **76**, no. 6, F353–F371, doi: [10.1190/geo2010-0359.1](https://doi.org/10.1190/geo2010-0359.1).
- Edwards, R., 1997, On the resource evaluation of marine gas hydrate deposits using sea-floor transient electric dipole-dipole methods: *Geophysics*, **62**, 63–74, doi: [10.1190/1.1444146](https://doi.org/10.1190/1.1444146).
- Eidesmo, T., S. Ellingsrud, L. M. MacGregor, S. Constable, M. C. Sinha, S. Johansen, F. N. Kong, and H. Westerdahl, 2002, Sea bed logging (SBL), a new method for remote and direct identification of hydrocarbon filled layers in deepwater areas: *First Break*, **20**, 144–152.
- Ellingsrud, S., T. Eidesmo, S. Johansen, M. C. Sinha, L. M. MacGregor, and S. Constable, 2002, Remote sensing of hydrocarbon layers by seabed logging (SBL): Results from a cruise offshore Angola: *The Leading Edge*, **21**, 972–982, doi: [10.1190/1.1518433](https://doi.org/10.1190/1.1518433).
- Everett, M., and R. Edwards, 1993, Transient marine electromagnetics: The 2.5-D forward problem: *Geophysical Journal International*, **113**, 545–561, doi: [10.1111/gji.1993.113.issue-3](https://doi.org/10.1111/gji.1993.113.issue-3).
- Farquharson, C., and D. Oldenburg, 2004, A comparison of automatic techniques for estimating the regularization parameter in nonlinear inverse problems: *Geophysical Journal International*, **156**, 411–425, doi: [10.1111/gji.2004.156.issue-3](https://doi.org/10.1111/gji.2004.156.issue-3).
- Flekkoy, E., T. Holten, E. Haland, and K. Maloy, 2010, Extracting the signal from the noise in marine EM measurements: 72nd EAGE Conference and Exhibition, Extended Abstracts.
- Golub, G., and C. Van Loan, 1996, *Matrix computations*, 3rd ed.: The Johns Hopkins University Press.
- Gribenko, A., and M. Zhdanov, 2007, Rigorous 3D inversion of marine CSEM data based on the integral equation method: *Geophysics*, **72**, no. 2, WA73–WA84, doi: [10.1190/1.2435712](https://doi.org/10.1190/1.2435712).
- Holten, T., E. Flekkøy, B. Singer, E. Blixt, A. Hanssen, and K. Måløy, 2009, Vertical source, vertical receiver electromagnetic technique for offshore hydrocarbon exploration: *First Break*, **27**, 89–93.
- Kelley, C., 1999, *Iterative methods for optimization*: SIAM.
- Newman, G., and M. Commer, 2010, Joint electromagnetic-seismic inverse modeling for matched data resolution: Electromagnetic, Gravity, and Magnetic International Workshop, Extended Abstracts.
- Newman, G. A., and M. Commer, 2005, New advances in three-dimensional transient electromagnetic inversion: *Geophysical Journal International*, **160**, 5–32, doi: [10.1111/gji.2005.160.issue-1](https://doi.org/10.1111/gji.2005.160.issue-1).
- Scholl, C., and R. Edwards, 2007, Marine downhole to seafloor dipole-dipole electromagnetic methods and the resolution of resistive targets: *Geophysics*, **72**, no. 2, WA39–WA49, doi: [10.1190/1.2434775](https://doi.org/10.1190/1.2434775).
- Um, E., 2011, Three-dimensional finite-element time-domain modeling of the marine controlled-source electromagnetic method: Ph.D. dissertation, Stanford University.
- Um, E., and D. Alumbaugh, 2007, On the physics of the marine controlled-source electromagnetic method: *Geophysics*, **72**, no. 2, WA13–WA26.
- Um, E., J. Harris, and D. Alumbaugh, 2010, 3D time-domain simulation of electromagnetic diffusion phenomena: A finite-element electric-field approach: *Geophysics*, **75**, no. 4, F115–F126, doi: [10.1190/1.3473694](https://doi.org/10.1190/1.3473694).
- Weidelt, P., 2007, Guided waves in marine CSEM: *Geophysical Journal International*, **171**, 153–176, doi: [10.1111/gji.2007.171.issue-1](https://doi.org/10.1111/gji.2007.171.issue-1).
- Weiss, C., 2007, The fallacy of the “shallow-water problem” in marine CSEM exploration: *Geophysics*, **72**, no. 6, A93–A97, doi: [10.1190/1.2786868](https://doi.org/10.1190/1.2786868).